# Elastomers Fail from the Edge

Nan Xue[1,2,3] Rong Long,[4] Eric R. Dufresne,[1,2,3,*] and Robert W. Style[1,†]

[1]*Department of Materials, ETH Zürich, 8093 Zürich, Switzerland*
[2]*Department of Materials Science and Engineering, Cornell University, Ithaca, New York 14853, USA*
[3]*Laboratory of Atomic and Solid-State Physics, Cornell University, Ithaca, New York 14853, USA*
[4]*Department of Mechanical Engineering, University of Colorado Boulder, Boulder, Colorado 80309, USA*

The performance of soft devices is limited by the fracture resistance of elastomers. Thus, understanding how fracture resistance changes with material and sample geometry is an important challenge. A key observation is that thicker elastomers can be significantly tougher than thinner ones. We show that this surprising toughness enhancement in thick samples emerges from the 3D geometry of the fracture process. In contrast to the classical picture of a 2D crack, failure is driven by the growth of two separate "edge" cracks that nucleate early on at a sample's sides. As loading is increased, these cracks propagate in towards the sample midplane. When they merge, samples reach their ultimate failure strength. In thicker samples, edge cracks need to propagate farther before meeting, resulting in increased sample toughness. We demonstrate that edge-crack growth is controlled by the elastomer's strain-stiffening properties. Our results have direct implications for how to effectively toughen elastomers by controlling their geometry and large-strain mechanical properties.

Subject Areas: Materials Science, Mechanics, Soft Matter

## I. INTRODUCTION

Soft elastomers can undergo large and reversible deformations [1,2], making them useful in many fields ranging from soft robotics [3,4] to stretchable electronics [5,6]. In each of these applications, a key consideration is how the elastomers fail via fracture [7,8]. In stiff materials, such as glass and metals, established theories allow one to predict failure of both brittle and ductile materials in arbitrary geometries, based on the results of a few standard mechanical tests [8–10]. However, the same is not true of fracture in highly stretchable materials [11–26]. Here, the challenge originates from the large deformation near the tip of a crack, which leads to nonlinear stress and strain fields as well as complex failure and dissipation processes near the crack tip [1,2,27]. Our current understanding of soft fracture is based on a classical picture of essentially 2D crack growth. This picture is augmented by the emerging consensus that the crack-tip fracture process is controlled by two material length scales: the size of the crack-tip

failure zone where microscopic damage occurs and the size of the nonlinear zone where nonlinear elasticity dominates the deformation [1,2,28–30]. The relative size of these compared to each other, and in comparison to sample dimensions (e.g., thickness and crack length), is believed to dictate fracture behavior.

In this work, we reveal that this 2D picture does not capture the behavior of strain-stiffening elastomers. Specifically, we show that the surprising toughness enhancement of such elastomers arises from the three-dimensional structure of the fracture front. In particular, the fracture process involves the interaction of three independent cracks: one inner crack, and two edge cracks that grow inward from the faces of the sample. Ultimately, the sample toughness is determined by how much stretch can be applied before the edge cracks meet and merge at the sample's midplane. In thicker samples, edge cracks meet at a larger stretch than in thinner samples. Thus, the former are significantly tougher. Further, we show that thickness-dependent behavior is governed by a dimensionless parameter reflecting the strain-stiffening characteristic of an elastomer.

## II. THICKER ELASTOMERS ARE TOUGHER THAN THINNER ONES

In a standard fracture test, we rely on results being thickness independent to justify the measurement of material properties [1,23,31–33]. However, the fracture process in soft elastomers can be surprisingly thickness
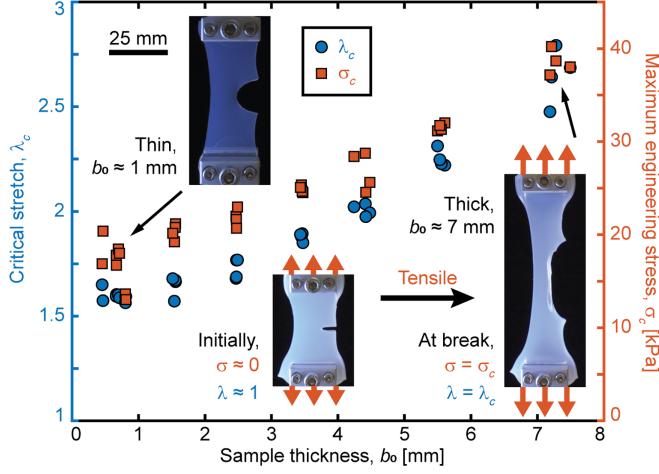
*[*]eric.r.dufresne@cornell.edu
[†]robert.style@mat.ethz.ch

FIG. 1.    Thicker elastomers are effectively tougher. We show the critical stretch $\lambda_c$ (blue circles) and maximum engineering stress $\sigma_c$ (red squares) of samples measured in single-edge-notch tension tests, as a function of the sample thickness $b_0$. Stress $\sigma$ is calculated by dividing the applied force by the initial cross-sectional area of unnotched samples, while $\lambda$ is calculated by dividing the current sample length by its initial length. Test samples are 30.5 mm $\times$ 25 mm $\times$ $b_0$ (length $\times$ width $\times$ thickness). The initial crack length is 10 mm, cut with a razor blade.

dependent [21,24,34,35] (Fig. 1). We perform single-edge-notch tension tests on samples of a commercial, highly stretchable silicone elastomer, Ecoflex 00-30 (Smooth-On) (see Sec. VIII for details). These samples have identical dimensions, other than thickness $b_0$, which we vary between 0.5 mm and 7.5 mm: a typical range for materials used in soft devices. Figure 1 shows the ultimate tensile strength (i.e., maximum engineering stress) $\sigma_c$ and the corresponding stretch $\lambda_c$ for samples tested to failure (typical $\sigma$–$\lambda$ curves are shown in Fig. 6, and the corresponding values of fracture energy are given in Fig. 10). Interestingly, thicker samples are more than twice as tough as thinner samples. This trend is opposite to that found in metals and glass, where thinner samples are tougher [8,36]. Alongside changes in $\sigma_c$ with $b_0$, we also see changes in crack morphology (Fig. 1, Supplemental Movies 1 and 2) [21]. Thinner samples exhibit classical Mode-I fracture while thicker samples have extremely blunted crack tips. This blunting has been attributed to the phenomenon of "sideways cracking" [21], where the crack path curves to travel parallel to the direction of applied tension.

## III. DYNAMIC IMAGING OF FRACTURE SURFACE GROWTH

To understand why our results are so thickness dependent, we image the fracture surface across the sample thickness as the sample is loaded. This process is facilitated by the use of a T-peel geometry [1,24,33,37,38], as shown in Fig. 2(a), which allows us to use a large range of thicknesses (widths), $b_0$, ranging from 1 mm to 25 mm. Samples are formed in a

mold containing a thin, metal sheet, which separates the two legs of the samples. The sheet is removed after curing, eliminating the need to cut an initial crack in the sample (see Sec. VIII). Samples are clamped at a distance of $15.9 \pm 0.3$ mm from the initial crack front on each of the legs. Then, we initiate the test at a grip-to-grip separation of $L_0 = 30.5 \pm 0.1$ mm. We increase the grip-to-grip stretch $\lambda$ at a rate of $\dot{\lambda} = 0.007$ s$^{-1}$, which is slow enough that viscoelastic rate effects will be negligible (see rheology in Ref. [39], and the appendixes).

To directly visualize the creation of a new fracture surface, we coat the sample with a dense layer of graphite powder so that the new crack surface can be easily identified by a lack of graphite. Upon stretching, this area lies essentially flat in the $y$-$z$ plane, so we always record images along the $x$ direction [the coordinate axis is defined in Fig. 2(a)]. During loading, the newly generated interface is bright and clearly visible, as seen in the example in Fig. 2(b) (Supplemental Movie 3). Importantly, this area is almost always symmetric about the midline of the sample [dashed line in Fig. 2(b)]. Thus, for compactness, we only show half of our images when presenting the results.

Our images show that cracks evolve in a highly non-uniform manner across a sample's thickness. For example, Figs. 2(c)–2(e) show how a new surface appears for a sample with $b_0 = 25$ mm. The crack first opens uniformly across the width of the sample (see image at $\lambda = 2.4$). However, as the stretch increases ($\lambda = 3$), the new surface is generated much faster at the outer edges of the crack. Later ($\lambda = 3.6$), the crack growth accelerates near the midplane of the sample. Perhaps surprisingly, crack growth is almost never up-down symmetric [e.g., Fig. 2(e)]. This asymmetry reflects the presence of "sideways" cracking mentioned above [21], which deflects the crack front either toward the $+y$ or $-y$ directions. Here, we always orient images so that cracks appear to deflect upward.

Cracks open uniformly near the midplane while having an edge structure that expands with a fixed shape. Figure 2(f) shows the shape of the bottom boundary of the developing crack at different stretches [colored curves in Figs. 2(c)–2(e)]. We superpose these shapes by plotting them relative to the lowest point on the curves. Interestingly, the shapes collapse onto a single curve near the edge. Outside of this boundary layer, the profile levels off, adopting a uniform opening at the center. With a further stretch, the boundary layer propagates deeper into the sample (see also Fig. 2 in Supplemental Material [40]). We borrow the term "boundary layer" from fluid mechanics, where flow profiles are uniform away from a surface but are strongly affected by viscosity in a thin layer adjacent to the surface [41,42]. In a similar fashion, the current boundary layer suggests a transition of the governing physics from the edge to the middle of the crack.

The boundary-layer structure is not only independent of stretch but also of sample thickness. Figures 3(a)–3(e)
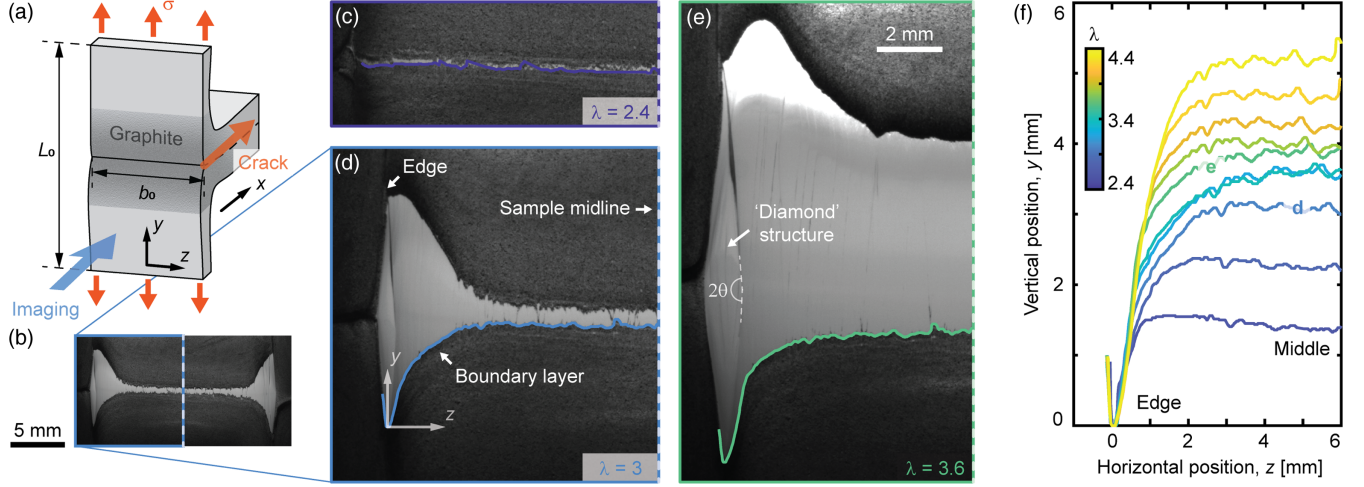
FIG. 2. Imaging new fracture surface in T-peel tests. (a) Schematic of the T-peel tests. (b) Typical image of new fracture surface (the dark area is graphite powder, and the bright area is the new fracture surface). All tests are symmetric about their midline (white, dashed line) to a good approximation. Here, $b_0 = 25$ mm. (c)–(e) Images of the left half of the same crack at increasing stretch: $\lambda = 2.4$, 3, and 3.6. The solid, colored curves denote the bottom boundaries of the new opening area. (f) Curves of the bottom boundaries of the crack opening area at different stretches collapsing onto a single curve near the sample edge, reminiscent of a boundary layer in fluid mechanics.

(taken from Supplemental Movies 3–7) show crack shapes in samples of different thicknesses, at the same edge opening, $L_{\mathrm{edge}} = 8$ mm. For all but the thinnest samples, the boundary-layer structures have the same shape near their tips, as demonstrated by plotting all the lower-boundary curves together [Fig. 3(f)]: a V shape with a well-defined root angle. For thinner samples, the boundary layers from the opposite edges of the crack overlap, and the variation in the crack opening from the edge to the midline becomes less pronounced. The independence of the boundary-layer shape from the sample thickness and applied stretch suggests that it is governed by a material property. We test this hypothesis by visualizing the failure of a different material (Dragon Skin 30, Smooth-On; see

Fig. 3 in Supplemental Material [40] and Supplemental Movie 8). There, we find a similar, stretch-independent boundary-layer structure but with a different profile.

## IV. THREE-DIMENSIONAL STRUCTURE OF THE FRACTURE SURFACE

The above boundary layer is actually the consequence of a structure that extends across the edge of the newly formed fracture surface, creating a diamond shape [e.g., Figs. 2(d) and 2(e), and Fig. 4 in Supplemental Material [40] ]. The bottom vertex of the diamond coincides with the V-shaped tip of the boundary layer. The width of the diamonds increases as the boundary layers
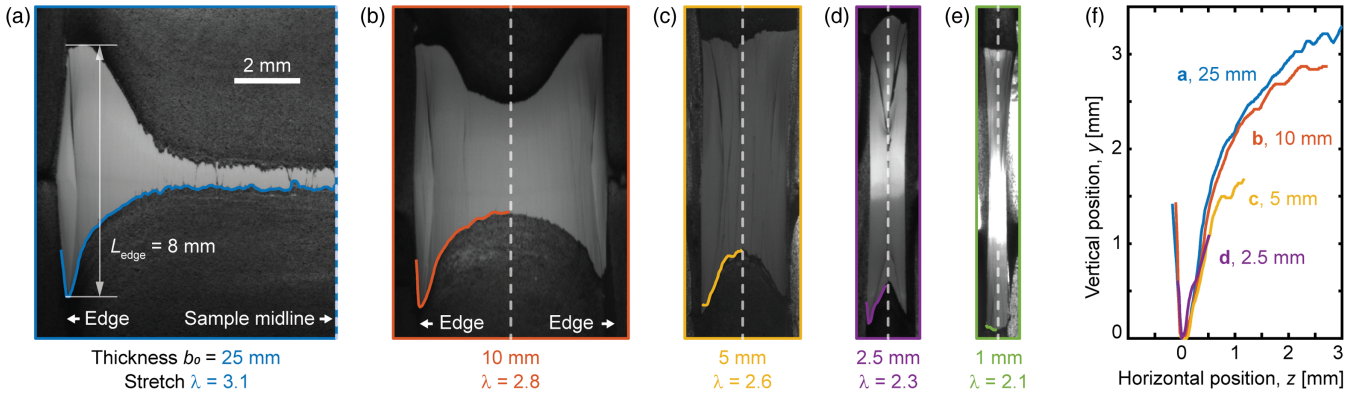


FIG. 3. Structure of boundary layers with different sample thicknesses. (a)–(e) Crack opening areas for samples with a range of different thicknesses $b_0$ at the same edge opening length: $L_{\mathrm{edge}} = 8$ mm. The continuous curves denote the bottom boundaries of the crack opening area, highlighting the boundary-layer shape. Dashed lines denote the vertical midlines of the samples. (f) Bottom-boundary shapes from panels (a)–(d) collapsing onto a single curve near the sample edge, supporting the idea of a well-defined boundary-layer structure that arises during fracture.
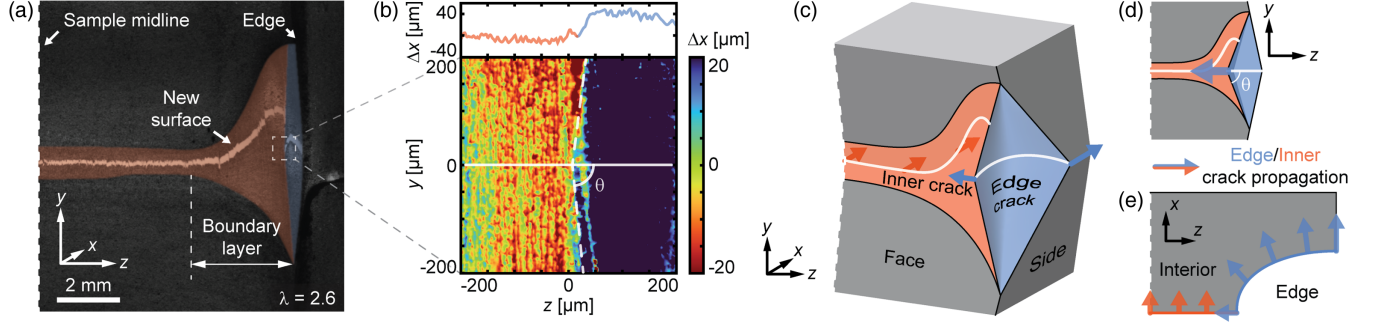
FIG. 4. Fracture surface generated by three distinct cracks: an inner crack and two edge cracks. (a) Recoating of a fracture surface with graphite powder after it has started to grow, which allows us to see the position of the crack tip (bright area). This surface is discontinuous, showing that there are multiple cracks that grow into the sample simultaneously. Inner cracks create the red-shaded opening area near the midplane of the sample. Edge cracks create the diamond-shaped, blue-shaded area on the edges of the sample. (b) Bottom: 3D profile of the crack surface around the position where the edge-crack tip meets the inner crack. Top: linescan of the surface topology along the white solid line in the bottom image (passing through the edge-crack tip). Dashed white lines indicate the boundary between the cracks, and $\theta$ is half the edge-crack tip-opening angle. (c) Three-dimensional schematic of the crack geometry. White curves show the crack tips while arrows indicate local directions of crack propagation. (d),(e) The $y$-$z$ and $x$-$z$ projections of the schematic in (c).

grow in toward the sample midplane. To characterize the diamond shapes, we measure the obtuse, internal angle $2\theta$ nearest to the midplane [see Figs. 2(e) and 3 in Supplemental Material [40]]. Similar to the boundary-layer structure, $\theta$ is independent of the sample thickness and applied stretch but dependent on the material. For Ecoflex, we find that $\theta = 86 \pm 1°$, while for Dragon Skin, $\theta = 79 \pm 2°$ (details can be found in Sec. VIII).

The diamond structures are actually distinct edge cracks. We show this by first growing the fracture surface under an increasing stretch until $\lambda = 3$ and then reapplying a graphite powder coating after unloading the sample. Upon further stretching, a new, bright area shows us the exact position of the crack tip [Fig. 4(a) and Supplemental Movie 9]. In the classical view of the fracture, the new opening area would be a single horizontal line. Instead, intriguingly, the crack tip is highly curved and discontinuous [Fig. 4(a)]. Across the majority of the thickness of the sample, there is a single opening strip, which curves upward as it approaches the sample sides before abruptly stopping when reaching the diamond-shaped feature. A new opening area then appears inside the diamond structure, cutting almost straight across its waist. This observation suggests that there are actually three separate crack fronts across the sample thickness: one inner crack and two edge cracks. The inner crack generates a new surface area across the middle of the sample [red-tinted area in Fig. 4(a)] while the edge cracks generate the diamond structures at the sample edges (blue-tinted area).

We visualize the transition from the inner crack to the edge crack by imaging the stretched surface with an optical profilometer. Figure 4(b) (bottom) shows the 3D sample surface at the inner end of the edge crack [dashed box in Fig. 4(a)]. The blue area in this figure is the area created by the edge crack. A height profile along the white line is shown at the top of the figure. Both the inner-crack and

edge-crack opening areas predominantly lie flat in the $y$-$z$ plane. However, the edge crack cuts deeper into the sample, as evidenced by the clear step in the surface profile at the interface between the two crack opening areas.

Altogether, our observations suggest an overall 3D crack-tip morphology in Fig. 4(c), with corresponding 2D projections in Figs. 4(d) and 4(e). Neglecting the "sideways" crack propagation in the $y$ direction, the inner crack propagates predominantly in the $x$ direction while the edge crack propagates in the $x$ and $z$ directions. The tip of the diamond corresponds to the tip of the edge crack [Fig. 4(d)], with a total opening angle $2\theta$.

## V. EDGE CRACKS PROPAGATE FIRST

Inner and edge cracks grow at different applied stretches. This finding is clearly seen by comparing the edge and midplane opening lengths, $L_{edge}$ and $L_{mid}$, at different levels of stretch in different samples [e.g., Fig. 5(a)]. Just after uniform initiation across the whole sample [i.e., at the point shown in Fig. 2(c)], $L_{edge}$ and $L_{mid}$ maintain similar small values [yellow regions of Figs. 5(b)–5(c). Then, the edge cracks start to propagate rapidly while the inner crack stays stationary (white region). After a lag, the inner crack starts to propagate (green region). This lag is larger in thicker samples. To quantify this case, we measured the sample stretch at the onset of crack propagation, $\lambda_{on}$, determined by extrapolating the rapid linear growth regime back to zero length [see Fig. 5(c)]. The onsets of edge- and inner-crack propagation are shown for a range of sample thicknesses in Fig. 5(d).

Interestingly, the onset of edge-crack propagation appears to be independent of thickness while inner cracks require larger stretches to propagate in thicker samples. Edge cracks start to propagate at a constant stretch of about 2, independent of $b_0$. This finding suggests that
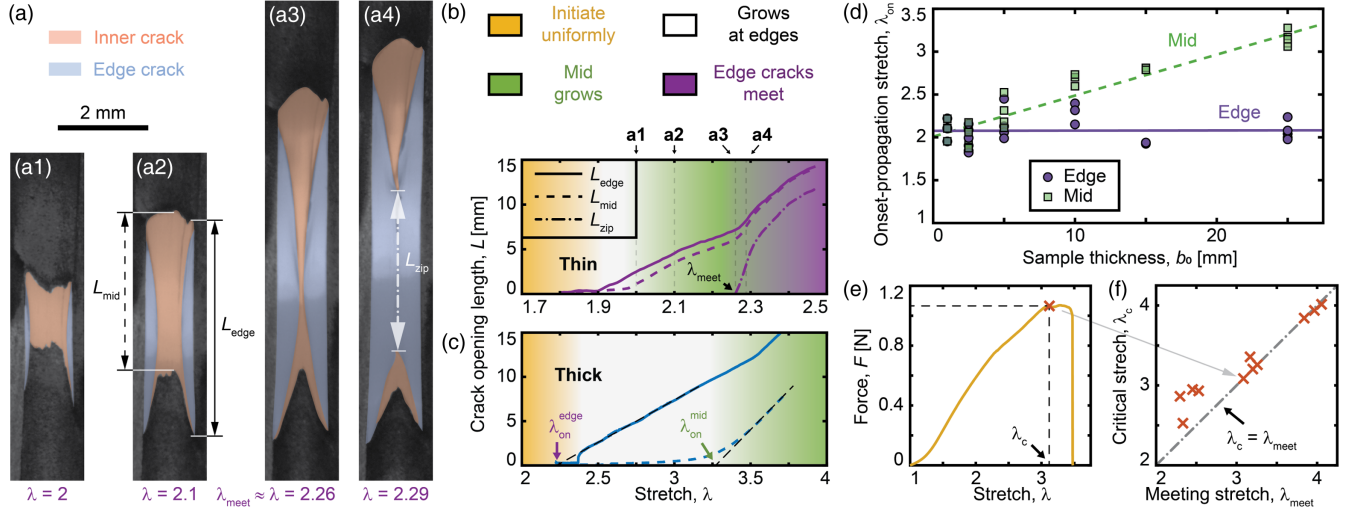
FIG. 5. Quantitative characterization of crack growth. (a) Evolution of inner (red) and edge (blue) cracks for a sample with $b_0 = 2.5$ mm. (b),(c) Crack opening lengths—$L_{edge}$, $L_{mid}$, and $L_{zip}$ (continuous, dashed, and dash-dotted lines, respectively)—for thin ($b_0 = 2.5$ mm) and thick ($b_0 = 25$ mm, Fig. 2) samples. Time points shown in panel (a) correspond to the points marked a1–a4 in panel (b). Different colored regions indicate the four stages of crack growth. Yellow: A thin crack opens uniformly across the sample. White: Edge cracks nucleate and start to grow. Green: The inner crack starts to grow. Purple: Edge cracks meet at the sample midplane. We extract effective stretches at the onset of crack propagation, $\lambda_{on}$, with a linear fit to the initial stages of crack growth [e.g., dashed black lines in panel (c)]. (d) Stretches at the onset of crack propagation for edge cracks (circles) and the crack at the sample midplane (squares) as a function of the sample thickness $b_0$. Lines show the best linear fits to the data sets. (e) Typical force-stretch curve ($b_0 = 5$ mm, Supplemental Movie 5). The force increases with stretch until reaching a maximum plateau at a critical stretch $\lambda_c$. (f) Stretch at maximum force, $\lambda_c$, as a function of the stretch at which the edge cracks meet at the sample midplane, $\lambda_{meet}$. The dash-dotted line is $\lambda_c = \lambda_{meet}$.

edge cracks are strictly associated with the surface. By contrast, the onset of inner-crack propagation increases linearly with thickness, which suggests that the onset of inner-crack propagation is affected by the inward propagation of edge cracks.

## VI. EDGE CRACKS MERGE AT THE POINT OF SAMPLE FAILURE

The samples fail when the edge cracks meet, at a stretch $\lambda_{meet}$. At this point, under displacement-controlled loading, the two edge cracks "zip" together. The length of the boundary between the two edge cracks, $L_{zip}$ [e.g., Fig. 5(a)], is plotted as a function of stretch in Fig. 5(b). The zipping of edge cracks accelerates the opening of the new fracture surface, indicated by the kinks in the curves of $L_{mid}$ and $L_{edge}$ at this point. Crucially, the force applied to the sample either abruptly plateaus or drops off when edge cracks meet [Figs. 5(e) and 13]. Indeed, when we plot the stretch at which the maximum force is attained, $\lambda_c$, against $\lambda_{meet}$ [Fig. 5(f)], we find that these are highly correlated. Thus, edge-crack meeting defines the sample's load-bearing capacity.

These results suggest an empirical criterion for failure, based on the meeting of edge cracks. Given the consistent diamond shape of the edge cracks, the distance they move inward is proportional to the edge-crack opening. Ignoring corrections due to the Poisson effect, edge cracks reach the midplane when $L_{edge} \approx b_0 \tan \theta$, about $10b_0$ for Ecoflex. Conveniently, data in Figs. 5(b)–5(d) show that the edge-crack opening is linear with the stretch above the onset of propagation. Thus, $L_{edge}/L_0 \approx c(\lambda - \lambda_{on}^{edge})$, where $c$ is a constant of $O(1)$ that depends weakly on the material and thickness (Fig. 14), and $L_0$ is the initial grip-to-grip distance of the sample. Combining these results, we find that $\lambda_c \approx \lambda_{on}^{edge} + b_0 \tan \theta/(cL_0)$. This failure criterion increases linearly with thickness, consistent with our observations in single-edge-notch tension (Fig. 1) and T-peel tests [Figs. 5(d) and 14].

The form of this failure criterion highlights the importance of the ratio $b_0/L_0$ in determining sample toughness. When $b_0/L_0 \gtrsim (\tan \theta)^{-1}$ (thick samples), edge cracks need to propagate significantly before meeting in the midplane. This process leads to higher critical stretches and enhanced fracture resistance. By contrast, when $b_0/L_0 \ll (\tan \theta)^{-1}$ (thin samples), edge cracks meet as soon as they form, and failure occurs at $\lambda_{on}^{edge}$, independent of thickness. In other words, we should obtain thickness-independent fracture results—a lack of geometric toughening—when the ratio of sample thickness to initial crack length is smaller than $(\tan \theta)^{-1}$. Extending this argument, we would expect effective toughening of the sample whenever any of the ratios given by $b_0$ divided by the various sample dimensions are comparable to, or larger than, $(\tan \theta)^{-1}$. This prediction is consistent with our data [Fig. 10(b)]:

For Ecoflex samples, we start to see effective toughening for $b_0 > L_0/\tan\theta \approx 2$ mm.

We also expect to obtain thickness-independent results in the limit of very thick samples [24]. Then, the stress in the middle of the samples will become high enough to cause ultimate failure of the sample center, before edge cracks meet. In this case, the toughness should plateau at a value that represents the plane-strain toughness [24], which matches the behavior we see in calculated toughness values for peel tests [Fig. 10(b)].

## VII. STRAIN-STIFFENING CONTROLS EDGE-CRACK BEHAVIOR

Our proposed criterion for thickness-dependent failure is based on two experimental observations: (1) Edge cracks propagate at a lower stretch than the inner crack, and (2) edge cracks maintain a consistent diamond shape. Both of these facts can be rationalized by reinterpreting some previous results of fracture mechanics for nonlinear-elastic materials.

Cracks propagate more easily at the edge because they concentrate stress more severely there. This finding follows from the fact that, for a range of nonlinear-elastic materials, the analytical, crack-tip stress singularity in a deformed sample is stronger for plane stress (i.e., edge cracks) than for plane strain (i.e., inner cracks) (see Ref. [27] and the appendixes). Thus, edge cracks fail first. The opposite behavior is seen in metals, where cracks grow first in the middle [8,43–45]. Here, plasticity controls fracture, and failure occurs earlier under plane-strain conditions, due to the high triaxial stress state that promotes void growth and coalescence.

The robust diamond shape of the edge cracks follows from the material's nonlinear-elastic behavior: In sufficiently strain-stiffening materials, crack tips take wedgelike shapes with a constant opening angle $2\theta$. Tensile tests reveal that the two silicones used in this study are strain stiffening and well fit by an exponential model with the strain-energy density function $W = \mu J_{\mathrm{m}}[e^{(I_1-3)/J_{\mathrm{m}}}-1]/2$ (Fig. 9). Here, $\mu$ is the shear modulus, $I_1$ is the trace of the right Cauchy-Green deformation tensor, and $J_{\mathrm{m}}$ is a dimensionless material parameter [17,46]. This case reduces to the familiar Neo-Hookean energy density in the limit of large $J_{\mathrm{m}}$. For Ecoflex and Dragon Skin, $J_{\mathrm{m}} = 36.5 \pm 0.4$ and $14 \pm 2$, respectively (Fig. 9). These values control the crack-tip angle $\theta$ as theory predicts that $\tan\theta = \alpha J_{\mathrm{m}}^{3/4}$, where $\alpha$ is an $O(1)$ constant (see Refs. [27,47] and the appendixes). Indeed, we find consistent values for our materials: For Ecoflex, $\alpha^{\mathrm{Eco}} = 0.9 \pm 0.2$, and for Dragon Skin, $\alpha^{\mathrm{Dra}} = 0.7 \pm 0.3$.

These results suggest that strain stiffening controls edge-crack behavior. We highlight this fact by replacing $\tan\theta$ in our criterion for when we expect thickness-dependent failure—now this is expected to occur when $b_0/L_0$ or

any of the ratios of thickness to sample dimension are greater than or around $J_{\mathrm{m}}^{-3/4}$. Furthermore, we reinforce the key role played by strain stiffening by performing tests on a non-strain-stiffening material (with Vytaflex 40 polyurethane, Smooth-On [48]). There, we observe no diamond structure (Fig. 5 in Supplemental Material [40]).

## VIII. CONCLUSIONS

In conclusion, we have shown that the results of the fracture tests on strain-stiffening elastomers can be thickness dependent, even for "thin" samples such as might be used in standard tests. Reversing the familiar thickness dependence of metals or glass, thicker elastomers are effectively tougher than thinner ones [24]. The underlying cause is the strain stiffening of the material, which leads to a fracture surface comprised of three independent cracks: An inner crack initiates first but propagates slowly; two diamond-shaped edge cracks have a delayed initiation but propagate more easily. When the edge cracks meet at the sample midplane, the sample fails.

Our observations of fracture being controlled by the interaction of multiple 3D cracks suggest that the classical 2D view of fracture is an oversimplification for elastomers. Indeed, an interesting question is what generates this 3D, multicrack structure [49]. We anticipate that this issue may have connections to recent work on secondary crack formation, for example, as caused by additional shear at a crack tip [16,26,50]. Furthermore, the emerging view of soft-solid fracture revolving around two material length scales—the sizes of the failure and nonlinear-elastic zones [2]—seems to be insufficient to describe the fracture process. For reference, for the Ecoflex elastomer studied here, these length scales are $O(0.1)$ mm and $O(1)$ mm, respectively (see appendixes). We have shown that a proper description of the fracture response needs to go beyond these material length scales and incorporate a dimensionless strain-stiffening parameter, such as $J_{\mathrm{m}}$. It is this strain-stiffening response that governs the behavior of the edge cracks that, crucially, govern sample failure.

Our results also suggest geometrical design considerations for increasing the toughness of a sample of a given elastomer. Thinner samples should have a lower, thickness-independent fracture resistance while thicker samples should be significantly tougher. We expect the cross-over to occur when the sample thickness increases above the smallest lateral sample dimension divided by $J_{\mathrm{m}}^{3/4}$. Challenges for future work include validation of our results over a wider class of strain-stiffening materials and the impact of related phenomena, like strain-induced crystallization [21,51]. While $J_{\mathrm{m}}$ reveals how long a material can survive after the onset of propagation of an edge crack, a complete understanding of the failure of these materials requires elucidation of the factors that drive edge-crack initiation and their onset of propagation.
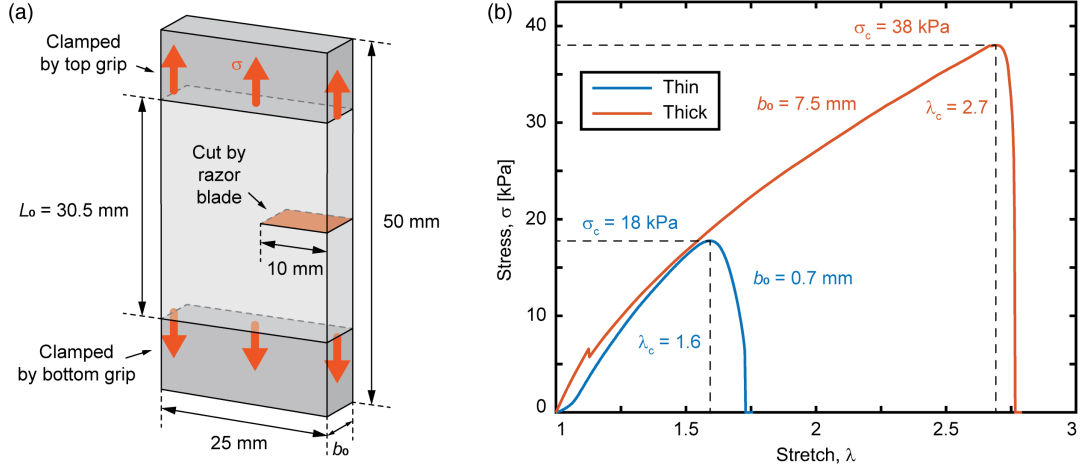
FIG. 6. Single-edge-notch test results. (a) Schematic of the samples used in the tests. The initial crack (red area) is cut with a razor blade. (b) Stress-stretch curves for tests on thin ($b_0 = 0.7$ mm, Supplemental Movie 1) and thick ($b_0 = 7.5$ mm, Supplemental Movie 2) samples. For each curve, the maximum value of the stress $\sigma_c$ and the corresponding stretch $\lambda_c$ are indicated by dashed lines. The thicker sample is more than twice as tough as the thinner one.

## IX. MATERIALS AND METHODS

### A. Preparation and curing of elastomers

We create Ecoflex 00-30 (Smooth-On) and Dragon Skin 30 (Smooth-On) samples by successively mixing together the two components (parts A and B) in a 1:1 ratio, degassing, and curing at 40 °C for 24 hours. Before mixing the components together, they are centrifuged at $10^4\times$ gravity for 4 hours to remove any large clumps of suspended silica particles. This process minimizes sample heterogeneity. Samples are used within 12 hours after finishing curing. Vytaflex 40 (Smooth-On) samples are simply mixed in a 1:1 ratio and allowed to cure at room temperature for 24 hours.

### B. Fracture experiments

Single-edge-notch tension specimens are created by curing slabs of Ecoflex 00-30 in Petri dishes and cutting out the desired shapes [see Fig. 6(a)]. These specimens are tested with a tensile-testing machine (Stable Micro Systems, TA.XTPlus, 5 kg load cell). The initial grip-to-grip distance is $L_0 = 30.5 \pm 0.1$ mm, and tests are performed at a constant stretch rate of $\dot\lambda = 0.007$ s$^{-1}$ [e.g., Fig. 6(b)].

T-peel samples are cured in a laser-cut acrylic mold containing a 50-µm-thick molybdenum sheet (see Fig. 7 and Fig. 1 in Supplemental Material [40]) that separates the two sample legs. The use of this sheet avoids the need for cutting the samples to form an initial crack. The sheet is removed after curing, and then the legs of the sample are clamped in the tensile-testing machine for testing. For thin samples ($b_0 \leq 2.5$ mm), we remove excess weight from the back of the sample with a razor blade (see the dashed line in Fig. 7).

We image a new fracture surface by coating graphite powder (5 µm, Sigma-Aldrich) on the sample surfaces with a brush. These surfaces are imaged with a camera (Thorlabs, SC1280G12M) with a telecentric lens (Seiwa Optical, FXL-0305-VT-165, 0.3×). The sample is imaged in transmission with an LED panel placed behind the sample. The 3D profile of the crack surface in Fig. 4(b) is measured with a 3D optical profilometer (S-neox, Sensoscan, 20 × objective). Here, no graphite powder is applied, and the sample is directly stretched to $\lambda = 2.6$.

Edge-crack opening angles $2\theta$ are measured in T-peel experiments with 21 measurements from four experiments with $b_0 = 10$ mm or 25 mm (Ecoflex) and with 16 measurements from four experiments with $b_0 = 20$ mm (Dragon Skin).

In this work, we always control the macroscopic stretch rate $\dot\lambda = 0.007$ s$^{-1}$. This stretch rate is slow [21] so that the viscoelasticity is negligible [39]. As control experiments, we perform three separate tests for the stretch rate $\dot\lambda = 0.03$ s$^{-1}$ and 0.001 s$^{-1}$, respectively (Fig. 8). Indeed, a lower stretch rate allows more time for crack growth, but the observed boundary layers and diamond structures are very similar.
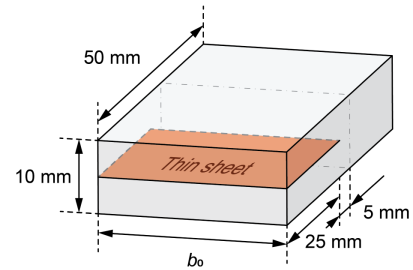


FIG. 7. T-peel test sample preparation. The schematic shows the mold used for sample preparation. A thin sheet placed in the mold during curing (red area) separates the "legs" of the sample.
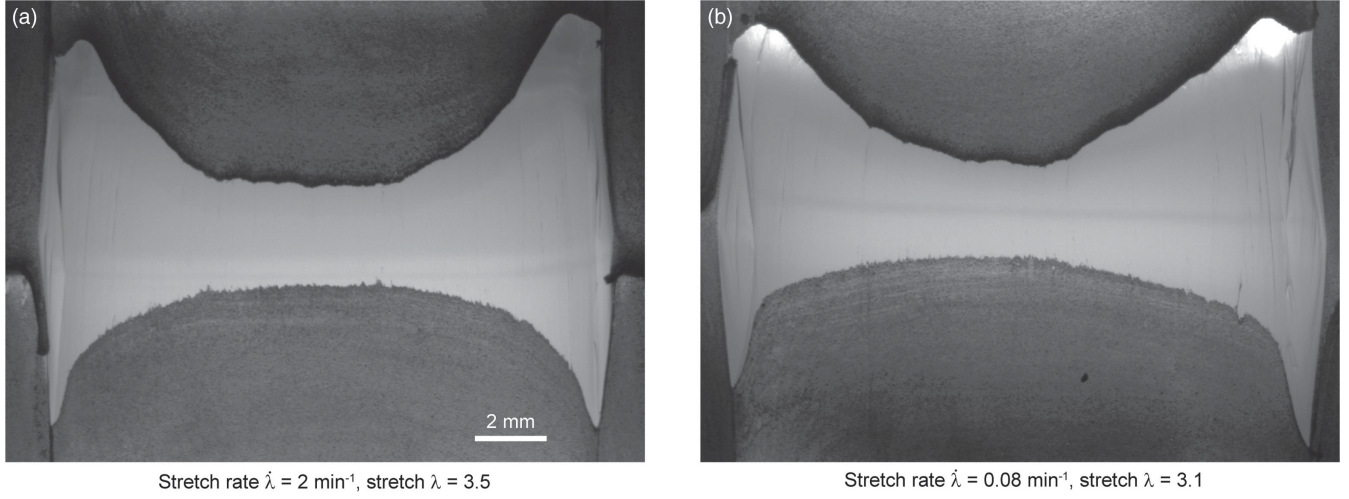
Stretch rate $\dot{\lambda}$ = 2 min$^{-1}$, stretch $\lambda$ = 3.5

Stretch rate $\dot{\lambda}$ = 0.08 min$^{-1}$, stretch $\lambda$ = 3.1

FIG. 8. T-peel tests performed on Ecoflex 00-30 at (a) high ($\dot{\lambda} = 0.03$ s$^{-1}$) and (b) low stretch rates ($\dot{\lambda} = 0.001$ s$^{-1}$), respectively. In both images, the sample thickness $b_0 = 25$ mm. Both experiments show boundary-layer structures and diamond-shaped edge cracks.
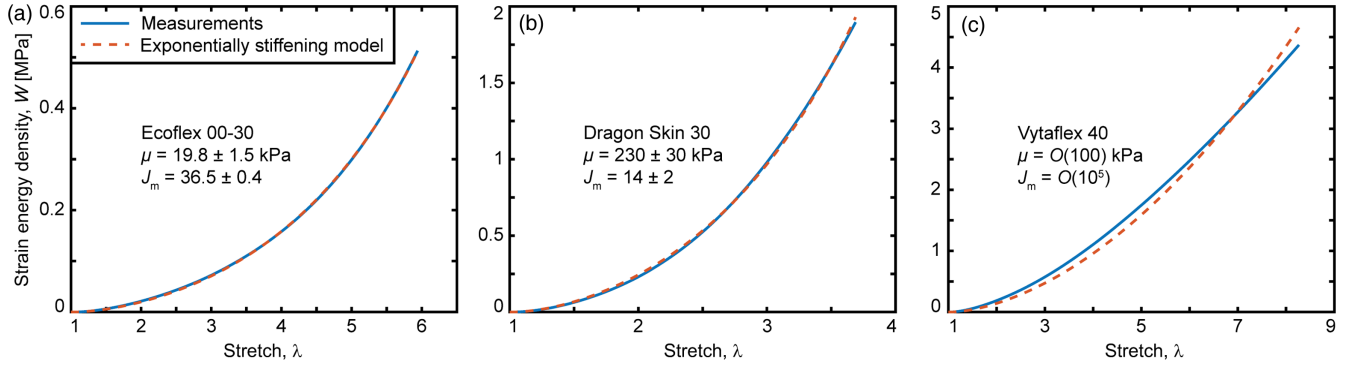


FIG. 9. Measuring the strain-stiffening properties of our materials with uniaxial tensile tests. Here, we plot strain-energy density $W$ as a function of $\lambda$, for (a) Ecoflex 00-30, (b) Dragon Skin 30, and (c) Vytaflex 40, respectively. The blue solid curves show the measured values of $W(\lambda)$ (see Sec. VIII for details). The red dashed curves show the best fit to the exponentially stiffening model given in the main text—the best-fit parameters are reported in the panels. Both Ecoflex 00-30 and Dragon Skin 30 are strain stiffening, as we see from the fact that $J_m$ is $O(10)$. Vytaflex 40 shows no evidence of strain stiffening, as $J_m$ is very large. Indeed, the fit implies that the elastomer needs to be stretched to $\lambda = O(10^4)$, far beyond its limit of breaking, to see a significant stiffening effect.

### C. Strain stiffening

We characterize strain-stiffening properties with multiple uniaxial tensile tests on rectangular samples. The samples are approximately 12.5 mm wide and 1.5 mm thick (cut by a razor blade), and clamped in the tensile-testing machine with an initial grip-to-grip distance of $L_0 = 15.5$ mm. Samples are stretched at a constant stretch rate $\dot{\lambda} = 0.007$ s$^{-1}$, and we calculate the strain-energy density $W(\lambda) = \int_1^\lambda \sigma d\lambda$, where $\sigma$ is the engineering stress and $\lambda$ is the stretch. This finding is then fitted to the exponential model given in the main text by setting $I_1 = \lambda^2 + 2/\lambda$ (see examples in Fig. 9).

### ACKNOWLEDGMENTS

### APPENDIX A: ESTIMATION OF FRACTURE ENERGY

In this work, our primary focus is on the critical stretch and maximum engineering stress as key parameters in the fracture resistance of elastomers. Here, we present an estimation of the fracture energy of the samples. Given
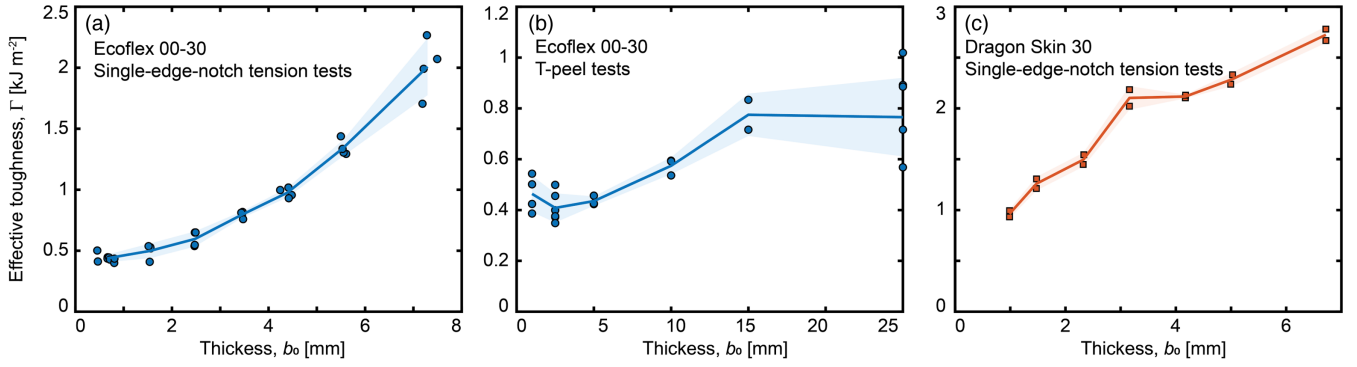
FIG. 10. Estimation of effective toughness for (a) Ecoflex 00-30 in single-edge-notch tension tests, (b) Ecoflex 00-30 in T-peel tests, and (c) Dragon Skin 30 in single-edge-notch tension tests, respectively. The solid lines represent the average, and the shaded areas indicate the standard deviation of the data.

the quasistatic propagation of the crack, it is reasonable to equate the fracture energy $\Gamma$ with the energy release rate $G$.

For single-edge-notch tension tests, an estimation of the energy release rate $G$ is given by [31,33]

$$G = \frac{6}{\sqrt{\lambda_c}} W(\lambda_c) c, \tag{A1}$$

where $\lambda_c$ is the critical stretch at the maximum engineering stress, $W(\lambda_c)$ is the strain-energy density of an untracked sample under the uniaxial stretch $\lambda_c$, and $c = 10$ mm is the notch length. The calculated effective fracture energy for Ecoflex 00-30 and Dragon Skin in single-edge-notch tension tests is shown in Figs. 10(a) and 10(c), respectively.

For T-peel tests, the energy release rate $G$ is estimated as [33]

$$G = \frac{2\lambda_c F_{\max}}{b_0} - 2W(\lambda_c)H_0, \tag{A2}$$

where $\lambda_c$ is the critical stretch at maximum force $F_{\max}$, and $H_0 = 5$ mm is the width (height) of the legs of the sample. The calculated fracture energy for Ecoflex 00-30 in T-peel tests is presented in Fig. 10(b).

It should be noted that Eqs. (A1) and (A2) are approximations for estimating the energy release rate $G$. One reason for this is because cracks can propagate "sideways" in tests, unlike the forward propagation assumed in deriving these equations. Furthermore, Eq. (A1) is an approximation, but the resulting errors are expected to be less than or around 5% [52].

Figure 10(a) demonstrates that in single-edge-notch tension tests, the effective fracture energy $\Gamma$ appears to plateau at a finite value at small $b_0$, and it increases monotonically with increasing $b_0$. For reference, our work suggests that this plateau should occur for $b_0 \lesssim c(\tan\theta)^{-1} \approx 1$ mm. This finding supports our observation that thicker elastomers are tougher due to the

increased distance edge cracks must travel to meet and cause sample failure.

For T-peel tests [Fig. 10(b)], the effective fracture energy again takes a finite value for small $b_0$ before increasing and then plateauing again at a large thickness ($b_0 \gtrsim 15$ mm). For reference, our work suggests that the toughness should take a constant value for $b_0 \lesssim L_0(\tan\theta)^{-1} \approx 2$ mm. This constant value (0.4–0.6 kJ m$^{-2}$) is consistent with the corresponding limiting value for single-edge-notch tension tests (0.5 kJ m$^{-2}$). The plateau at large $b_0$ closely aligns with the results of Ref. [24] and can be interpreted as follows: At larger thicknesses $b_0$, even though edge cracks grow towards the middle of the sample with increasing stretch, the stress at the center is sufficiently high to fracture the sample directly, without the edge cracks meeting. In this scenario, the fracture resistance becomes independent of sample thickness, leading to a saturation in effective fracture energy. We anticipate a similar plateau in the effective fracture energy for thicker samples or smaller crack sizes in single-edge-notch tension tests. Interestingly, the finite value of toughness at small $b_0$ is in contrast to the results of Ref. [24], who reported that fracture energy appeared to be negligible as $b_0 \to 0$.

## APPENDIX B: PLANE STRESS VERSUS PLANE STRAIN

A highly stretchable elastomer breaks mainly at a high stress that elongates the material [27,47]. To rationalize the fact that the elastomer breaks more easily near the edge, we compare the Cauchy stress (i.e., true stress) component $\tau_{yy}$ directly ahead of the crack tip under plane-stress and plane-strain conditions. The coordinates and notations used are defined in Fig. 11. The plane stress is associated with the near-surface edge crack (note that this plane-stress condition is a 2D approximation of the 3D configuration near the edge [53]) while the plane strain is associated with the inner crack. We first use a neo-Hookean solid as an example and extend the result to other hyperelastic

(a)                              (b)

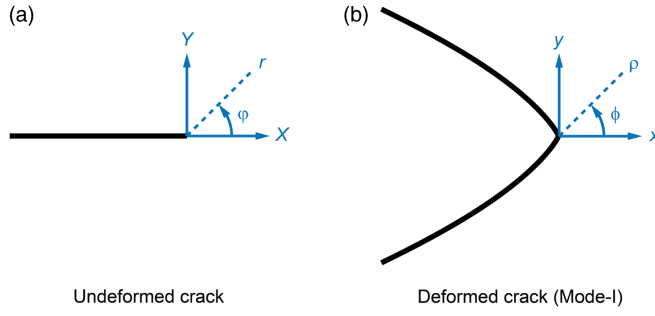Undeformed crack                 Deformed crack (Mode-I)

FIG. 11. Coordinates and notations that describe the configurations of the (a) undeformed crack and (b) deformed crack, respectively. The black curves denote the crack. The blue curves denote the coordinate systems.

models. All of the models used are incompressible (i.e., the Poisson ratio $\nu = 0.5$). The derivations presented here are primarily based on Ref. [27], which reviews the work from Refs. [47,54,55].

For a neo-Hookean solid, when expressed in terms of the reference (i.e., undeformed) polar coordinates $(r, \varphi)$, the first-order asymptotic solution of $\tau_{yy}$ is the same for plane-stress and plane-strain conditions [Eqs. (50) and (68) in Ref. [27]]:

$$\tau_{yy} = \frac{\mu}{4} a^2 r^{-1}, \tag{B1}$$

where $\mu$ is the shear modulus and $a$ is an undetermined constant representing the amplitude of the crack-tip stress field. Determination of $a$ requires the far-field boundary conditions away from the crack tip, such as the sample geometry and the applied loading. Equation (98) in Ref. [27] shows that $a$ can be related to the energy release rate $G$ through the $J$-integral approach as, for both plane stress and plane strain, $G = (\mu\pi a^2/4)$. Therefore, Eq. (B1) can be rewritten as

$$\tau_{yy} = \frac{G}{\pi} r^{-1}. \tag{B2}$$

Equation (B2) specifies the distribution of $\tau_{yy}$ around the crack tip with its amplitude governed by the energy release rate $G$. Note that $G$ can be evaluated using the external loading and sample dimensions; e.g., see Ref. [33] for $G$ of a T-peel test [Eq. (2.5)] and of a single-edge-notch tension test [Eq. (2.7)].

The difference between plane-stress and plane-strain solutions arises when we consider the distribution of $\tau_{yy}$ in the deformed configuration, i.e., in terms of $(\rho, \phi)$. For simplicity, we consider $\tau_{yy}$ directly ahead of the crack tip ($\varphi = 0$ and $\phi = 0$), motivated by the expectation that the mode-I crack tends to grow along this direction. The relations between $r$ and $\rho$ are [Eqs. (90a) and (93) in Ref. [27]]

$$\text{plane strain}: \rho = \frac{4}{3a} r^{3/2}, \tag{B3}$$

$$\text{plane stress}: \rho = c_0 r, \tag{B4}$$

where $c_0$ is an undetermined constant that will be discussed later. Substituting Eqs. (B3) and (B4) into Eq. (B2) gives

$$\text{plane strain}: \frac{\tau_{yy}}{\mu} = \left(\frac{2}{3}\right)^{2/3} \left(\frac{G}{\mu\pi}\right)^{2/3} \rho^{-2/3}, \tag{B5}$$

$$\text{plane stress}: \frac{\tau_{yy}}{\mu} = c_0 \frac{G}{\mu\pi} \rho^{-1}. \tag{B6}$$

Determination of the constant $c_0$ also requires the far-field boundary conditions: One needs to solve the deformation of the entire fracture sample, rather than merely performing asymptotic analysis in the vicinity of the crack tip. It is shown in Ref. [56] that $c_0 = O(1)$ through finite element simulations of a pure-shear fracture sample [Fig. 3(b) in Ref. [56]]. Nevertheless, Eqs. (B5) and (B6) show that the plane-stress condition results in a stronger stress singularity in the deformed configuration ($\tau_{yy} \sim \rho^{-1}$) than that of the plane-strain condition ($\tau_{yy} \sim \rho^{-2/3}$).

The underlying physical mechanism for the different singularities is the distinct stretch behavior along the $x$ direction. Directly ahead of the crack tip (at $\varphi = 0$), the stretch ratio $\lambda_x$ is [using Eqs. (B3) and (B4)]

$$\lambda_x = \frac{d\rho}{dr} = \begin{cases} 2r^{1/2}/a \equiv \lambda_x^{\text{PE}} & (\text{plane strain}) \\ c_0 \equiv \lambda_x^{\text{PS}} & (\text{plane stress}). \end{cases} \tag{B7}$$

Near the crack tip ($r \to 0$), the plane-strain solution of $\lambda_x$, denoted as $\lambda_x^{\text{PE}}$, approaches zero, indicating a severe contraction along the $x$ direction. In contrast, the plane-stress solution of $\lambda_x$, denoted as $\lambda_x^{\text{PS}}$, is a constant $c$ near the crack tip. Indeed, Ref. [56] shows that $c_0$ is even slightly larger than 1, indicating that there is a slight stretch along the $x$ direction. This difference can be rationalized as follows: (1) Under plane strain, the stretch along the out-of-plane direction is constrained, and there is a severe stretch along the $y$ axis. Therefore, to maintain incompressibility, the material must undergo severe contraction along the $x$ axis to conserve its volume. (2) Under plane stress, there is still a severe stretch along the $y$ axis, but the material is free to contract along the out-of-plane direction to conserve its volume. Therefore, it does not need to contract along the $x$ axis. Indeed, the out-of-plane contraction can lead to a valleylike surface profile near the tip of a deformed crack (which is also detected by our profilometer scanning).

The severe lateral contraction under plane strain (i.e., $\lambda_x^{\text{PE}} \ll 1$) essentially squeezes the high-stress region further toward the crack tip, thereby reducing the stress singularity.

This effect can be mathematically expressed by defining the average lateral stretch:

$$\bar{\lambda}_x \equiv \frac{1}{r}\int_0^r \lambda_x dr = \frac{1}{r}\int_0^r \frac{d\rho}{dr}dr = \frac{\rho}{r}. \quad (B8)$$

Using Eq. (B8), we can rewrite Eq. (B2) as

$$\tau_{yy} = \frac{G}{\pi}\rho^{-1}\bar{\lambda}_x(\rho), \quad (B9)$$

where $\bar{\lambda}_x(\rho)$ means that $\bar{\lambda}_x$ can be a function of $\rho$. Since $\bar{\lambda}_x^{PE} \ll \bar{\lambda}_x^{PS}$, we can see that, at the same location $\rho$ ahead of the crack tip in the deformed configuration, $\tau_{yy}$ under plane strain is smaller than that under plane stress.

The physical mechanism described above should be applicable to all incompressible hyperelastic solids. For example, Ref. [27] lists the asymptotic solutions for a class of generalized neo-Hookean solids with the following strain-energy density function:

$$W = \frac{\mu}{2b}\left\{\left[1 + \frac{b}{n}(I_1 - 3)\right]^n - 1\right\}, \quad (B10)$$

where $b$ and $n$ are dimensionless material parameters and $I_1$ is the trace of the right Cauchy-Green deformation tensor. Here, $n$ controls the strain-stiffening behavior of the solid. Note that $n = 1$ corresponds to a neo-Hookean solid while $n > 1$ leads to stronger strain-stiffening behavior. For this class of materials, asymptotic analysis results in, again, the same first-order solution of $\tau_{yy}$ in terms of the reference polar coordinates $(r, \varphi)$ [Eqs. (46c) and (63) in Ref. [27]]. For simplicity, here we only look at the result directly ahead of the crack tip ($\varphi = 0$), where

$$\tau_{yy} = \frac{G}{n\pi}r^{-1}. \quad (B11)$$

Note that to obtain Eq. (B11), we have already replaced the undetermined coefficient $a$ by the energy release rate $G$ using the $J$ integral in Eqs. (97a) and (97b) in Ref. [27]. We consider the cases with moderate to strong strain stiffening and set $n > 3/2$, which allows us to obtain the following results [Eqs. (58a) and (92a) in Ref. [27]]:

$$\text{plane strain: } \rho = \frac{c_1}{a}r^{1+\frac{1}{2n}}, \quad (B12)$$

$$\text{plane stress: } \rho = \frac{c_2}{\sqrt{a}}r^{1+\frac{1}{4n}}, \quad (B13)$$

where $c_1$ and $c_2$ are of $O(1)$, weakly dependent on $n$. Using Eqs. (B11)–(B13), we find that $\tau_{yy} \sim \rho^{-(2n/2n+1)}$ for plane strain and $\tau_{yy} \sim \rho^{-(4n/4n+1)}$ for plane stress. For example, when $n = 2$, the stress singularity is $\tau_{yy} \sim \rho^{-0.8}$ for plane strain and $\tau_{yy} \sim \rho^{-0.89}$ for plane stress. Interestingly, the

difference in the singularity between plane stress and plane strain is smaller for strain-stiffening materials than that for neo-Hookean materials. This is because the strain-stiffening behaviors limit the amount of stretch along the $y$ axis near the crack tip and hence can reduce the contrast in $\lambda_x$ ahead of the crack tip.

How does the stress singularity affect the fracture process? The commonly adopted Griffith criterion involving energy release rate $G$ and fracture energy $\Gamma$ is not adequate for our discussion due to the lack of understanding on how $G$ or $\Gamma$ varies along the thickness direction. By asserting that the stronger stress singularity under plane stress promotes crack growth, we have implicitly assumed that crack growth is controlled by the Cauchy stress distribution around the crack tip in the deformed configuration. This finding is elaborated below.

In reality, stress cannot be infinite at the crack tip. The singular stress solution must break down at some point near the crack tip. For example, when the stress reaches a threshold to trigger damage, the material may deviate from its elastic stress-strain relation, and hence the singular asymptotic solution should break down. This case is manifested in the emergence of a material length scale near the crack tip, e.g., the crack-tip load-transfer length $\Gamma/W_*$ [2,28,30], where $W_*$ is the critical energy per unit volume for material failure. Within this length scale around the crack tip, the material undergoes failure. Understanding the precise events that occur within this fracture process zone remains an ongoing area of investigation. We propose that the stronger stress singularity under plane stress can intensify the fracture process zone in two possible ways: (1) If the size of the fracture process zone is a material constant, a stronger stress singularity would result in higher stress within the zone. (2) If the stress within the fracture process zone is constant (e.g., an intrinsic tensile strength), a stronger stress singularity would result in a larger zone size. Either of these ways facilitates the crack growth under plane-stress (i.e., edge-crack) conditions.

## APPENDIX C: EDGE-CRACK OPENING (DIAMOND) PROFILE

Our 3D picture of the crack morphology suggests that $\theta$ is exactly the crack-tip opening angle of the edge cracks [Fig. 4(d)]. There, our imaging direction is locally parallel to the edge-crack opening surface [i.e., we image the $y$-$z$ plane, Fig. 4(b)] and perpendicular to the local main propagation direction [the $x$ direction, Fig. 4(e)]. Furthermore, these near-surface cracks are subjected to symmetric tensile loading, motivating a comparison with analytical results for mode-I, plane-stress crack opening shapes. Previous solutions [e.g., Fig. 11(b) in Ref. [47]] suggest that, as one increases the degree of strain stiffening (by increasing $n$ in the generalized neo-Hookean model), the open profile of the crack transitions from a blunt, parabolic shape (for neo-Hookean, $n = 1$) to

a wedgelike shape (large $n$ or exponential model). The wedgelike edge-crack profile observed in our experiments motivates us to adopt the exponential model

$$W(\lambda) = \frac{\mu J_\mathrm{m}}{2}\left[\exp\left(\frac{I_1 - 3}{J_\mathrm{m}}\right) - 1\right], \qquad \text{(C1)}$$

where $J_\mathrm{m}$ is a dimensionless parameter that reflects the material's strain-stiffening property. To be consistent with our experiments, we employ the same coordinate notations as those presented in Fig. 4(d).

The first-order asymptotic solution of the crack opening profile for an exponentially stiffening solid is [Eq. (71a) in Ref. [27]]

$$y^* = z^*[-\ln z^*]^{1/4}\sqrt{-\ln\left(z^*[-\ln z^*]^{1/4}\right)} \equiv z^* f(z^*), \quad \text{(C2)}$$

where $y^*$ and $z^*$ are normalized coordinates to $(y, z)$ of the upper crack surface:

$$y^* = \frac{y}{A_2\sqrt{J_\mathrm{m}}} \quad \text{and} \quad z^* = \frac{J_\mathrm{m}^{1/4}z}{CA_2} \approx \frac{J_\mathrm{m}^{1/4}z}{A_2}. \quad \text{(C3)}$$

Here, $A_2$ is an undetermined constant specifying the amplitude of the asymptotic solution, and $C$ is a dimensionless constant close to 1 and hence is neglected. Though the crack opening profile in Eq. (C2) is not strictly a wedge since the slope $dy^*/dz^*$ changes as $z^*$ varies, we note that the function $[-\ln z^*]^{1/4}\sqrt{-\ln\left(z^*[-\ln z^*]^{1/4}\right)}$ is $O(1)$ unless $z^*$ is very small, due to the weak singularity of logarithmic functions. Here, we adopt a first-order approximation by setting this to 1 (the error will be discussed later), so Eq. (C2) becomes

$$y^* = z^*. \qquad \text{(C4)}$$

Substituting this into Eqs. (C3), we obtain

$$\tan\theta \equiv \frac{y}{z} = J_\mathrm{m}^{3/4}. \qquad \text{(C5)}$$

This is the equation we used to predict the half-angle of the edge-crack opening.

Next, we discuss the error in the approximation of Eq. (C2). These two solutions are directly compared in Fig. 12(a). Although the linear approximation captures the open angle of the crack profile given by Eq. (C2), it underestimates the opening angle. To quantify the discrepancy, we plot the factor that is neglected in Eq. (C2), i.e., $f(z^*) = y^*/z^*$, in Fig. 12(b). Depending on the value of $y^*$, the value of $f(z^*)$ is mainly from 1 to 5, indicating that the linear approximation might underestimate the value of $y^*/z^*$ by a few times. To obtain a better estimate, we note that in the experiments, $2\theta$ is always measured using the crack shape at $y = \pm 1$ mm. To obtain the corresponding $y^*$, we use Eq. (99) in Ref. [27], which links $A_2$ to the energy release rate $G$ through the $J$ integral:

$$A_2 = \frac{G}{\mu\pi}J_\mathrm{m}e^{3/J_\mathrm{m}}. \qquad \text{(C6)}$$

Since the edge crack undergoes propagation as the diamond structure expands, it is reasonable to set the energy release rate $G$ equal to the fracture energy $\Gamma$. For EcoFlex 00-30, $\Gamma$ is reported to be $O(100)$ Jm$^{-2}$ [57], in agreement with our estimation of effective toughness in Fig. 10. Given that the EcoFlex 00-30 used in our experiments is centrifuged before curing to remove large additives, our $\Gamma$ is potentially lower. Therefore, we estimate $\Gamma$ to be in the range of 10 to 500 Jm$^{-2}$. Using our measurements $\mu = 19.8$ kPa and $J_\mathrm{m} = 36.5$, we find that $A_2$ is within 6.4 to 320 mm. Calculated by Eq. (C3), the corresponding $y^*$ related to the measurement of the wedge angle is $y^* = 0.0005$ to 0.026. This range corresponds to
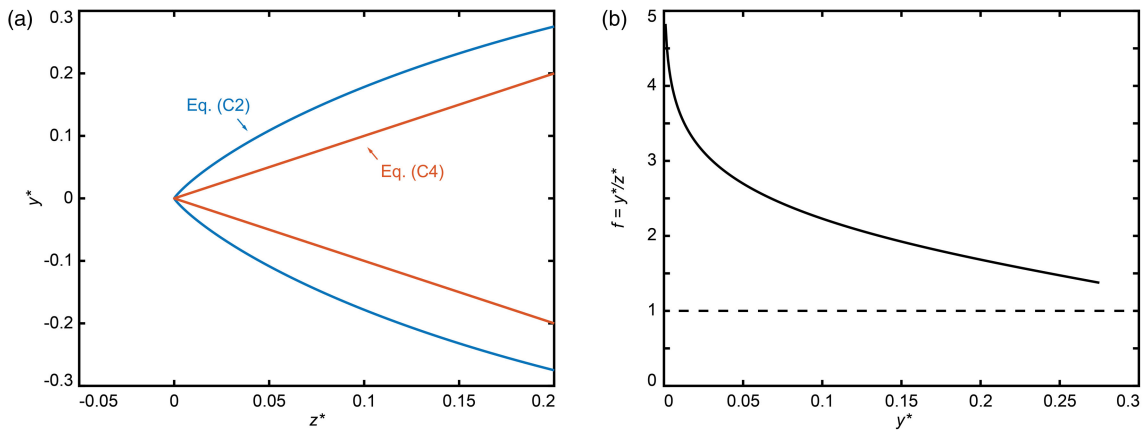


FIG. 12. First-order asymptotic solution of the crack opening profile for an exponentially stiffening solid. (a) Comparison of Eqs. (C2) (blue curves) and (C4) (red lines). (b) Error between Eqs. (C2) and (C4), $f = y^*/z^*$, as a function of $y^*$. Note that $f$ can be below 1 for $y^* \gtrsim 0.3679$ (where $z^* \gtrsim 0.3679$ as well).

$f(z^*) = 3.1$ to 5.1. Therefore, our approximation may underestimate the ratio by a factor of 3.1 to 5.1.

Moreover, it is important to point out that Eq. (C2) serves as the first-order asymptotic solution of the crack opening profile, while there are higher-order terms that are not included [33]. These higher-order terms could be important given the weak logarithmic singularity in the first-order term. Additionally, the detailed geometry of the edge cracks in our experiments could be more complex than what is simply accounted for under plane stress. To reflect these errors, we can add a dimensionless correction factor $\alpha$ to Eq. (C5), i.e.,

$$\tan \theta \equiv \frac{y}{z} = \alpha J_m^{3/4}, \tag{C7}$$

which indicates

$$\theta = \tan^{-1}(\alpha J_m^{3/4}). \tag{C8}$$

We expect that $\alpha = O(1)$. The linear approximation of Eq. (C2) suggests that $\alpha$ is within 3.1 to 4.3. However, due to the additional errors that are not quantifiable, we allow $\alpha$ to be undetermined. With all the considerations above, we expect to see the wedgelike crack tips for $J_m \lesssim 100$. Since $J_m = O(10)$ for many of the strain-stiffening materials, $\theta$ is usually close to 90°. Interestingly, setting $\alpha = 1$, Eq. (C8) is identical to Eq. (C5), and this predicts that $\theta = 86.1 \pm 0.3°$ and $82 \pm 1°$ for Ecoflex and Dragon Skin, respectively, which are in reasonable agreement with our measurements.
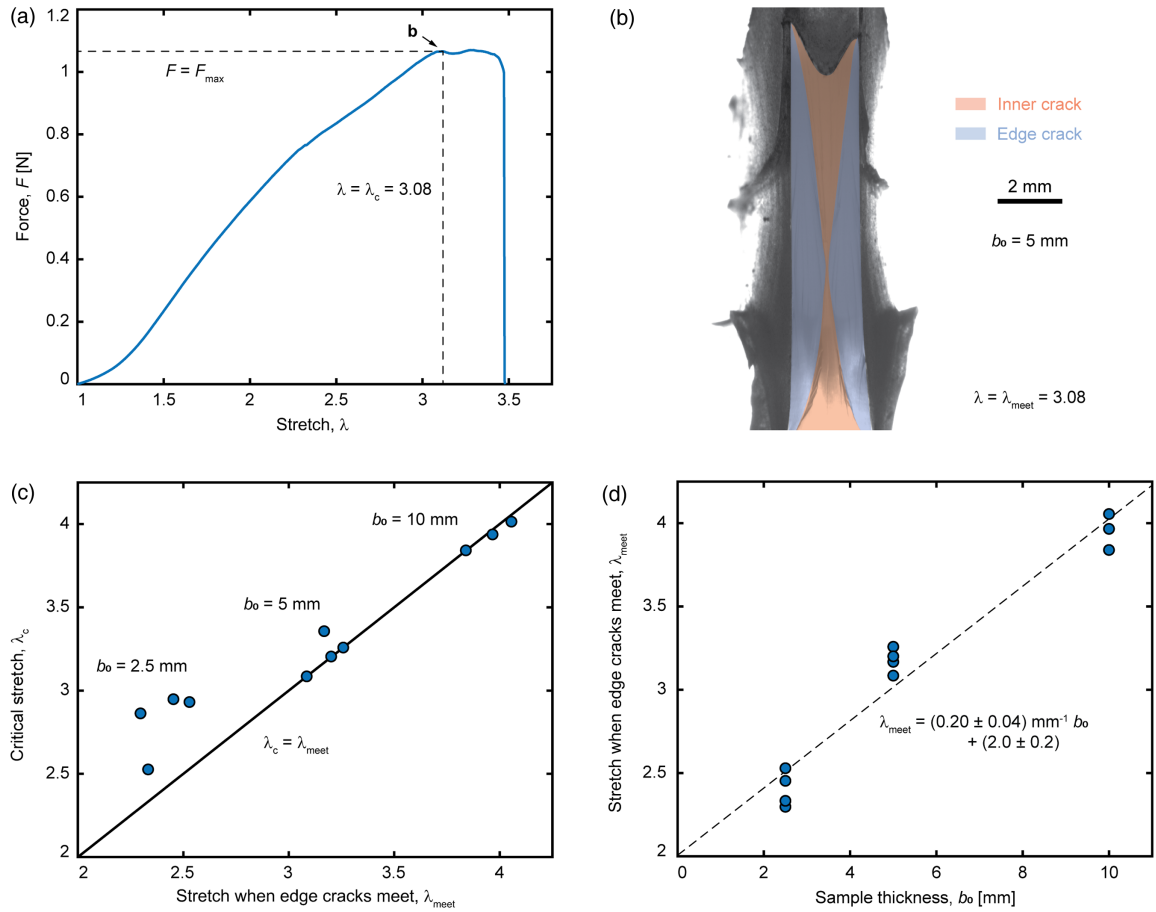


FIG. 13. Ultimate sample failure caused by edge-crack meeting. (a) Typical force-stretch curve for an Ecoflex 00-30, T-peel sample with $b_0 = 5$ mm (Supplemental Movie 5). The force increases with stretch, until reaching a maximum plateau at a critical stretch $\lambda_c = 3.08$. After the plateau, the force drops rapidly when the sample breaks. (b) Image, from the same experiment, showing the fracture surface at the point at which the two edge cracks (blue tinted) are just about to meet in the sample midplane. This meeting occurs at a stretch $\lambda_{meet} = 3.08$. (c) Plot of $\lambda_c$ versus $\lambda_{meet}$ for T-peel, Ecoflex 00-30 samples, with a range of thicknesses. The line shows $\lambda_{meet} = \lambda_c$. For thicker samples, $\lambda_{meet} = \lambda_c$ to an excellent approximation. For thinner samples, $\lambda_{meet}$ is usually slightly smaller than $\lambda_c$. In these samples, we see a sudden decrease in the slope of the force-stretch curve when the edge cracks meet, but the material can subsequently tolerate a little more stretch before it fully breaks. (d) The $\lambda_{meet}$ as a function of sample thickness $b_0$. The dashed line is the best linear fit. Because $\lambda_{meet}$ is larger for thicker samples, these samples will break at higher stretches than thinner samples.
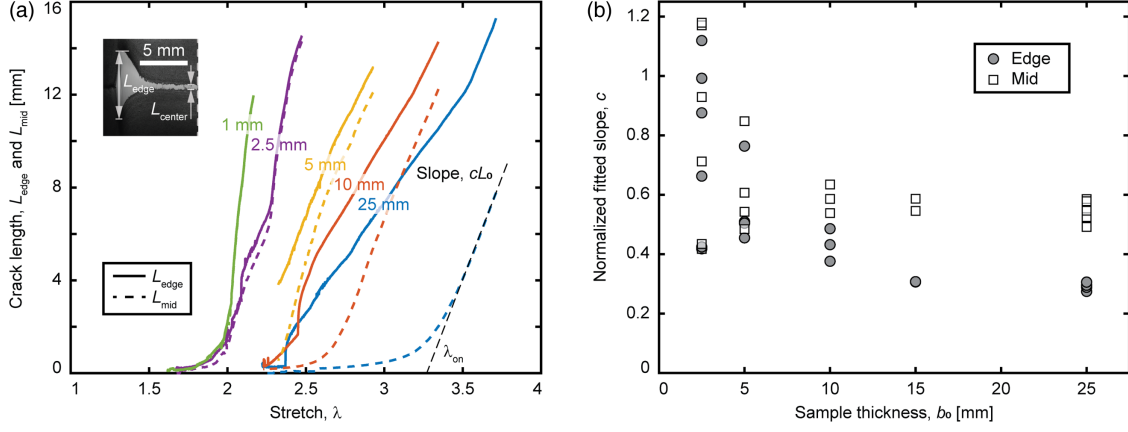
FIG. 14. Quantitative characterization of crack growth in T-peel tests. (a) Edge-crack opening length $L_{\mathrm{edge}}$ and midline opening length $L_{\mathrm{mid}}$ as a function of the stretch $\lambda$, for samples with a range of different thicknesses. The dashed black line at the bottom right shows an example of the linear fit of the crack growth, which we use to find the effective stretch at the onset of crack propagation, $\lambda_{\mathrm{on}}$ (see the main text for details). The slope of this line, $cL_0$, shows how fast the crack subsequently grows with stretch. Here, $L_0$ is the initial grip-to-grip distance of the T-peel test. (b) Normalized crack growth rate $c$ as a function of sample thickness $b_0$. The filled circles and unfilled squares denote $c_{\mathrm{edge}}$ and $c_{\mathrm{mid}}$, respectively. Note that $c$ is relatively constant for thick samples ($b_0 \gtrsim 10$ mm) but increases for thinner samples.

## APPENDIX D: SIZES OF THE FAILURE AND NONLINEAR-ELASTIC ZONES

According to Ref. [2], the size of the failure zone can be estimated as

$$\xi \sim \Gamma/W_*. \tag{D1}$$

For Ecoflex 00-30, we estimate that $\Gamma \approx 100$ Jm$^{-2}$ [57] and $W_* \approx 0.5$ MPa [Fig. 9(a)]. Thus, we have $\xi \approx 0.2$ mm. Note that $\xi$ mainly represents the length near the crack tip where the microscopic damage processes occur.

The size of the nonlinear-elastic zone can be estimated as

$$\ell \sim \Gamma/E, \tag{D2}$$

where $E \approx 3\mu$ is Young's modulus of the material. For Ecoflex 00-30, $\mu = 19.8 \pm 1.5$ kPa. Thus, we have $\ell \approx 2$ mm. Note that $\ell$ mainly represents the length near the crack tip where the nonlinear elasticity dominates the deformation. Substituting Eq. (D2) into Eq. (C6), we obtain

$$A_2 \sim \ell J_{\mathrm{m}}. \tag{D3}$$

Here, $A_2$ mainly represents the length near the crack tip, within which the wedgelike crack opening profile [Eq. (C2)] remains valid. Therefore, Eq. (D3) indicates that the diamond edge-crack structure lies in the nonlinear zone. This finding is consistent with our previous argument that the diamond structure is a consequence of the nonlinear-elastic (i.e., strain-stiffening) behavior of the material. However, to describe the structure of the edge crack, one needs to use $J_{\mathrm{m}}$, beyond the conventional

nonlinear-elastic zone size $\ell$. We note that $J_{\mathrm{m}}$ reflects the nonlinear characteristics of an elastomer's stress-strain curve, which is not accounted for by $\ell$. Here, $\ell$ reflects only the initial slope of the stress-strain curve.

[1] C. Creton and M. Ciccotti, *Fracture and adhesion of soft materials: A review*, Rep. Prog. Phys. **79**, 046601 (2016).

[2] R. Long, C. Y. Hui, J. P. Gong, and E. Bouchbinder, *The fracture of highly deformable soft materials: A tale of two length scales*, Annu. Rev. Condens. Matter Phys. **12**, 71 (2021).

[3] G. M. Whitesides, *Soft robotics*, Angew. Chem., Int. Ed. **57**, 4258 (2018).

[4] M. Cianchetti, C. Laschi, A. Menciassi, and P. Dario, *Biomedical applications of soft robotics*, Nat. Rev. Mater. **3**, 143 (2018).

[5] J. A. Rogers, T. Someya, and Y. Huang, *Materials and mechanics for stretchable electronics*, Science **327**, 1603 (2010).

[6] C. Yang and Z. Suo, *Hydrogel ionotronics*, Nat. Rev. Mater. **3**, 125 (2018).

[7] X. Zhao, *Multi-scale multi-mechanism design of tough hydrogels: Building dissipation into stretchy networks*, Soft Matter **10**, 672 (2014).

[8] T. L. Anderson, *Fracture Mechanics: Fundamentals and Applications* (CRC Press, Boca Raton, FL, 2017).

[9] A. A. Griffith, *VI. The phenomena of rupture and flow in solids*, Phil. Trans. R. Soc. A **221**, 163 (1921).

[10] D. S. Dugdale, *Yielding of steel sheets containing slits*, J. Mech. Phys. Solids **8**, 100 (1960).

[11] J. K. Knowles, *The finite anti-plane shear field near the tip of a crack for a class of incompressible elastic solids*, Int. J. Fract. **13**, 611 (1977).

[12] E. M. Arruda and M. C. Boyce, *A three-dimensional constitutive model for the large stretch behavior of rubber elastic materials*, J. Mech. Phys. Solids **41**, 389 (1993).

[13] A. N. Gent, *A new constitutive relation for rubber*, Rubber Chem. Technol. **69**, 59 (1996).

[14] H. Lakrout, P. Sergot, and C. Creton, *Direct observation of cavitation and fibrillation in a probe tack experiment on model acrylic pressure-sensitive-adhesives*, J. Adhes. **69**, 307 (1999).

[15] T. Baumberger, C. Caroli, and D. Martina, *Solvent control of crack dynamics in a reversible hydrogel*, Nat. Mater. **5**, 552 (2006).

[16] T. Baumberger, C. Caroli, D. Martina, and O. Ronsin, *Magic angles and cross-hatching instability in hydrogel fracture*, Phys. Rev. Lett. **100**, 178303 (2008).

[17] M. E. Seitz, D. Martina, T. Baumberger, V. R. Krishnan, C. Y. Hui, and K. R. Shull, *Fracture and large strain behavior of self-assembled triblock copolymer gels*, Soft Matter **5**, 447 (2009).

[18] E. Bouchbinder, *Dynamic crack tip equation of motion: High-speed oscillatory instability*, Phys. Rev. Lett. **103**, 164301 (2009).

[19] A. Livne, E. Bouchbinder, I. Svetlizky, and J. Fineberg, *The near-tip fields of fast cracks*, Science **327**, 1359 (2010).

[20] N. Bouklas, C. M. Landis, and R. Huang, *Effect of solvent diffusion on crack-tip fields and driving force for fracture of hydrogels*, J. Appl. Mech. **82**, 081007 (2015).

[21] S. Lee and M. Pharr, *Sideways and stable crack propagation in a silicone elastomer*, Proc. Natl. Acad. Sci. U.S.A. **116**, 9251 (2019).

[22] B. Zhang and S. B. Hutchens, *On the relationship between cutting and tearing in soft elastic solids*, Soft Matter **17**, 6728 (2021).

[23] C. Li, Z. Wang, Y. Wang, Q. He, R. Long, and S. Cai, *Effects of network structures on the fracture of hydrogel*, Extreme Mech. Lett. **49**, 101495 (2021).

[24] T. Yin, G. Zhang, S. Qu, and Z. Suo, *Peel of elastomers of various thicknesses and widths*, Extreme Mech. Lett. **46**, 101325 (2021).

[25] B. N. J. Persson, *A simple model for viscoelastic crack propagation*, Eur. Phys. J. E **44**, 3 (2021).

[26] M. Wang, M. Adda-Bedia, J. M. Kolinski, and J. Fineberg, *How hidden 3D structure within crack fronts reveals energy balance*, J. Mech. Phys. Solids **161**, 104795 (2022).

[27] R. Long and C. Y. Hui, *Crack tip fields in soft elastic solids subjected to large quasi-static deformation—A review*, Extreme Mech. Lett. **4**, 131 (2015).

[28] Z. P. Bažant, *Scaling of quasibrittle fracture: asymptotic analysis*, Int. J. Fract. **83**, 19 (1997).

[29] K. R. Shull and C. Creton, *Deformation behavior of thin, compliant layers under tensile loading conditions*, J. Polym. Sci. **42**, 4023 (2004).

[30] C. Chen, Z. Wang, and Z. Suo, *Flaw sensitivity of highly stretchable materials*, Extreme Mech. Lett. **10**, 50 (2017).

[31] H. W. Greensmith, *Rupture of rubber. X. The change in stored energy on making a small cut in a test piece held in simple extension*, J. Appl. Polym. Sci. **7**, 993 (1963).

[32] E. Ducrot, Y. Chen, M. Bulters, R. P. Sijbesma, and C. Creton, *Toughening elastomers with sacrificial bonds and watching them break*, Science **344**, 186 (2014).

[33] R. Long and C. Y. Hui, *Fracture toughness of hydrogels: Measurement and interpretation*, Soft Matter **12**, 8069 (2016).

[34] A. Kadir and A. G. Thomas, *Tear behavior of rubbers over a wide range of rates*, Rubber Chem. Technol. **54**, 15 (1981).

[35] G. J. Lake, C. C. Lawrence, and A. G. Thomas, *High-speed fracture of elastomers: Part I*, Rubber Chem. Technol. **73**, 801 (2000).

[36] ASTM E399-05, *Standard Test Method for Linear-Elastic Plane-Strain Fracture Toughness* $K_{IC}$ *of Metallic Materials*, (ASTM International, 2005), https://www.astm.org/e0399-05.html.

[37] R. S. Rivlin and A. G. Thomas, *Rupture of rubber. I. Characteristic energy for tearing*, J. Polym. Sci. **10**, 291 (1953).

[38] M. A. Haque, T. Kurokawa, and J. P. Gong, *Super tough double network hydrogels and their application as biomaterials*, Polymer **53**, 1805 (2012).

[39] D. R. Darby, Z. Cai, C. R. Mason, and J. T. Pham, *Modulus and adhesion of Sylgard 184, Solaris, and Ecoflex 00-30 silicone elastomers with varied mixing ratios*, J. Appl. Polym. Sci. **139**, e52412 (2022).

[40] See Supplemental Material at http://link.aps.org/supplemental/10.1103/PhysRevX.14.011054 for descriptions of the Supplemental Movies and more control experiments.

[41] L. Prandtl, *Über Flüssigkeits bewegung bei sehr kleiner Reibung*, Verhandl. III Int. Math. Kongr. **484**, 575 (1905).

[42] G. K. Batchelor, *An Introduction to Fluid Dynamics* (Cambridge University Press, Cambridge, England, 2000).

[43] R. von Mises, *Mechanik der festen Körper im plastisch-deformablen Zustand*, Nachr. d. Kgl. Ges. Wiss. zu Göttingen, Math.-Phys. Kl. **4**, 582 (1913), https://eudml.org/doc/58894.

[44] S. K. Kudari and K. G. Kodancha, *3D stress intensity factor and T-stresses (T11 and T33) formulations for a compact tension specimen*, Frat. ed Integrita Strutt. **11**, 216 (2017), https://www.fracturae.com/index.php/fis/article/view/1834.

[45] W. Lan, X. Deng, and M. A. Sutton, *Investigation of crack tunneling in ductile materials*, Eng. Fract. Mech. **77**, 2800 (2010).

[46] A. Cristiano, A. Marcellan, R. Long, C. Y. Hui, J. Stolk, and C. Creton, *An experimental investigation of fracture by cavitation of model elastomeric networks*, J. Polym. Sci. B **48**, 1409 (2010).

[47] R. Long, V. R. Krishnan, and C. Y. Hui, *Finite strain analysis of crack tip fields in incompressible hyperelastic solids loaded in plane stress*, J. Mech. Phys. Solids **59**, 672 (2011).

[48] S. Moser, Y. Feng, O. Yasa, S. Heyden, M. Kessler, E. Amstad, E. R. Dufresne, R. K. Katzschmann, and R. W. Style, *Hydroelastomers: Soft, tough, highly swelling composites*, Soft Matter **18**, 7229 (2022).

[49] S. Gvirtzman and J. Fineberg, *Nucleation fronts ignite the interface rupture that initiates frictional motion*, Nat. Phys. **17**, 1037 (2021).

[50] I. Kolvin, G. Cohen, and J. Fineberg, *Topological defects govern crack front motion and facet formation on broken surfaces*, Nat. Mater. **17**, 140 (2018).

[51] S. Trabelsi, P. A. Albouy, and J. Rault, *Stress-induced crystallization around a crack tip in natural rubber*, Macromolecules **35**, 10054 (2002).

[52] Z. Liu, M. Zakoworotny, J. Guo, A. T. Zehnder, and C.-Y. Hui, *Energy release rate of a single edge cracked specimen subjected to large deformation*, Int. J. Fract. **226,** 71 (2020).

[53] J. Steck, S. Hassan, and Z. Suo, *Fracture initiated from corners in brittle soft materials*, J. Mech. Phys. Solids **170,** 105115 (2023).

[54] R. A. Stephenson, *The equilibrium field near the tip of a crack for finite plane strain of incompressible elastic materials*, J. Elast. **12,** 65 (1982).

[55] P. H. Geubelle and W. G. Knauss, *Finite strains at the tip of a crack in a sheet of hyperelastic material: I. Homogeneous case*, J. Elast. **35,** 61 (1994).

[56] V. R. Krishnan, C. Y. Hui, and R. Long, *Finite strain crack tip fields in soft incompressible elastic solids*, Langmuir **24,** 14245 (2008).

[57] Y. Qi, Z. Zou, J. Xiao, and R. Long, *Mapping the nonlinear crack tip deformation field in soft elastomer with a particle tracking method*, J. Mech. Phys. Solids **125,** 326 (2019).

# Supplemental Material for "Thicker Elastomers are Tougher"

Nan Xue,[1,2,3] Rong Long,[4] Eric R. Dufresne,[1,2,3,*] and Robert W. Style[1,†]

[1]*Department of Materials, ETH Zürich, 8093 Zürich, Switzerland.*
[2]*Department of Materials Science and Engineering, Cornell University, Ithaca, NY, 14853, USA.*
[3]*Laboratory of Atomic and Solid-State Physics, Cornell University, Ithaca, NY, 14853, USA.*
[4]*Department of Mechanical Engineering, University of Colorado Boulder, Boulder, CO 80309, USA.*

(Dated: February 20, 2024)

## Thin sheets in the molds for consistent formation of the initial crack

The thin sheet in the mold is essential to the initiation of the crack. For the experiments reported in the article, we always use molybdenum sheets with a thickness of 50 $\mu$m. The molybdenum sheets are provided by Plansee and processed by ETH D-PHYS shop. The edge of the molybdenum sheet is sharp. Consequently, the crack is initially uniform across the thickness (width) of the sample [e.g., Fig. 2(c) in the article]. As control experiments, we test 200 $\mu$m-thick polyvinyl chloride (PVC) sheets (GBC HiClear) and 130 $\mu$m-thick polyester (PES) sheets (Avery Zweckform, 3566). We repeat tests of each type of thin sheet for three times, and the observations are robust. Examples are in Supplemental Material Figs. 1(b) and 1(c), and Supplemental Movies 11 and 12. The PVC sheet has two sharp corners at its edge, which leads to the formation of two separate sets of cracks [Supplemental Material Fig. 1(b)]. In contrast, the polyester sheet is blunted at its edge. As a result, we do not see any inner crack initiated near the mid-plane [Supplemental Material Fig. 1(c)]. Interestingly, the cracks with the polyester sheet are also an example that the direction of the crack's sideways growth can be different between the left edge and right edge. Based on this comparison, we choose the molybdenum sheets since they provide the simplest and most robust initial crack tips.

As control experiments, we also coat graphite and image the new surface in the single-edge-notch tension test. When we use a mold with a thin sheet to create the initial notch in the sample, the observation is very similar to the T-peel tests: the cracks start at the edges and grow toward the mid-plane of the sample. However, interestingly, when we use a razor blade to cut the initial notch, we sometimes observe that the crack initiates first near the mid-plane of the sample and then grows outward (there, the ultimate failure of the sample occurs when the diamond-shaped crack reaches the outer edge). This observation suggests that the cutting by a razor blade is less uniform and less controlled.

## SUPPLEMENTAL MOVIES

The supplemental movies for this manuscript include the following:

Movie 1. Single-edge-notch tension test of a thin sample. The sample thickness $b_0 = 0.7$ mm.

Movie 2. Single-edge-notch tension test of a thick sample. The sample thickness $b_0 = 7.5$ mm.

Movie 3. T-peel test until the sample breaks. The sample thickness $b_0 = 25$ mm.

Movie 4. T-peel test until the sample breaks. The sample thickness $b_0 = 10$ mm.

Movie 5. T-peel test until the sample breaks. The sample thickness $b_0 = 5$ mm.

Movie 6. T-peel test until the sample breaks. The sample thickness $b_0 = 2.5$ mm.

Movie 7. T-peel test until the sample breaks. The sample thickness $b_0 = 1$ mm.

Movie 8. T-peel test until the sample breaks. The material is Dragon Skin 30 (rather than Ecoflex 00-30). The sample thickness $b_0 = 20$ mm.

Movie 9. T-peel test. After unloading the sample at $\lambda = 3$, we re-coat and re-stretch the sample. The sample thickness $b_0 = 25$ mm.

Movie 10. T-peel test. The material is VytaFlex 40 (rather than Ecoflex 00-30), which is non-strain-stiffening. The sample thickness $b_0 = 25$ mm.

Movie 11. T-peel test until the sample breaks. While curing, we put a thin PVC sheet in the mold. The sample thickness $b_0 = 25$ mm.

Movie 12. T-peel test until the sample breaks. While curing, we put a thin polyester sheet in the mold. The sample thickness $b_0 = 25$ mm.

---

[*] eric.r.dufresne@cornell.edu

[†] robert.style@mat.ethz.ch
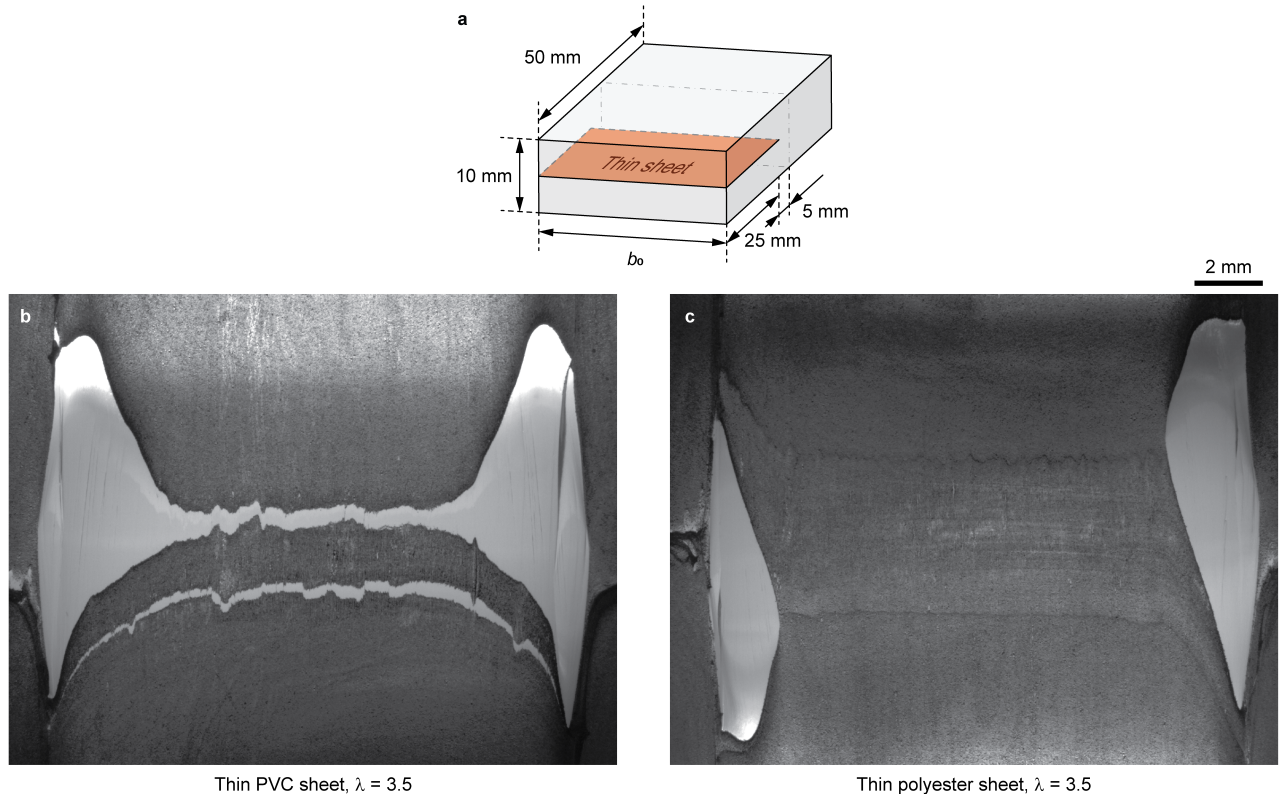
Supplemental Material Fig. 1. T-peel test sample preparation. (a) A schematic showing the mold used for sample preparation. A thin sheet placed in the mold during curing (red area) separates the 'legs' of the sample. (b),(c) In the article, we use thin molybdenum sheets that give a crack tip that is initially very sharp. Two other types of sheets are also tested as control experiments. (b) PVC sheets have two sharp edges, and this leads to two sets of cracks forming across the sample (Supplemental Movie 11). (c) Polyester sheets are blunted at the edge, and in this case, inner crack growth is delayed (Supplemental Movie 12). Here, edge cracks also grow asymmetrically.
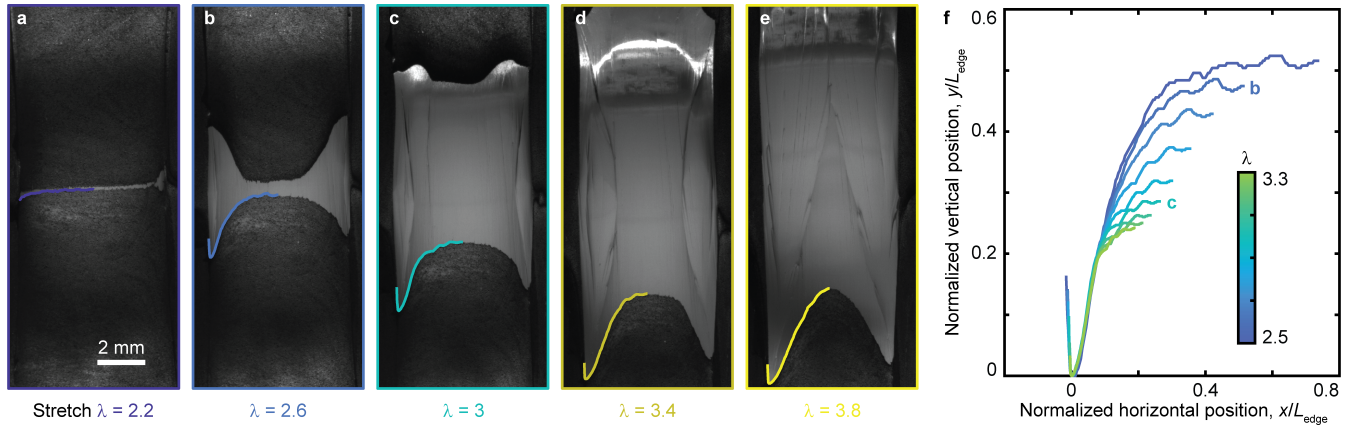


Supplemental Material Fig. 2. A further example of the growth of the boundary layer during a T-peel test on an Ecoflex 00-30 sample with thickness $b_0 = 10$ mm (see also Supplemental Movie 4). (a)–(e) A sequence showing growth of the fracture surface at regular stretch intervals. Continuous, colored curves denote the boundary layers of the new fracture surface. These curves collapse onto a single, V-shaped curve near the sample edge (f). In this case, we scale the curves by the crack opening length in the $y$ direction, $L_{\text{edge}}$. These collapse, like the un-scaled data, and additionally highlight how the inner crack is increasingly influenced by the boundary layer as stretch increases.
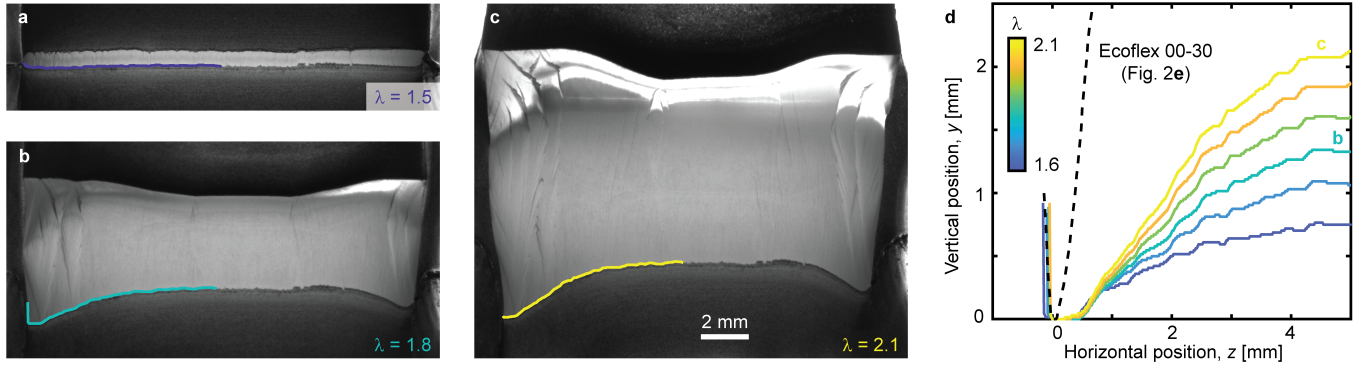
Supplemental Material Fig. 3. An example of the observed boundary layer structure during a T-peel test on a Dragon Skin 30 sample with thickness $b_0 = 20$ mm (Supplemental Movie 8). (a)–(c) A sequence showing growth of the fracture surface at regular stretch intervals. Continuous, colored curves denote the boundary layers of the new fracture surface. These curves collapse onto a single curve near the sample edge (d). For reference, the dashed curve shows the boundary layer shape measured in Ecoflex 00-30 [here, taken from the sample with $b_0 = 25$ mm, $\lambda = 3.6$ in Fig.2(e) in the article]. Interestingly, we observe secondary diamond structures in the crack.
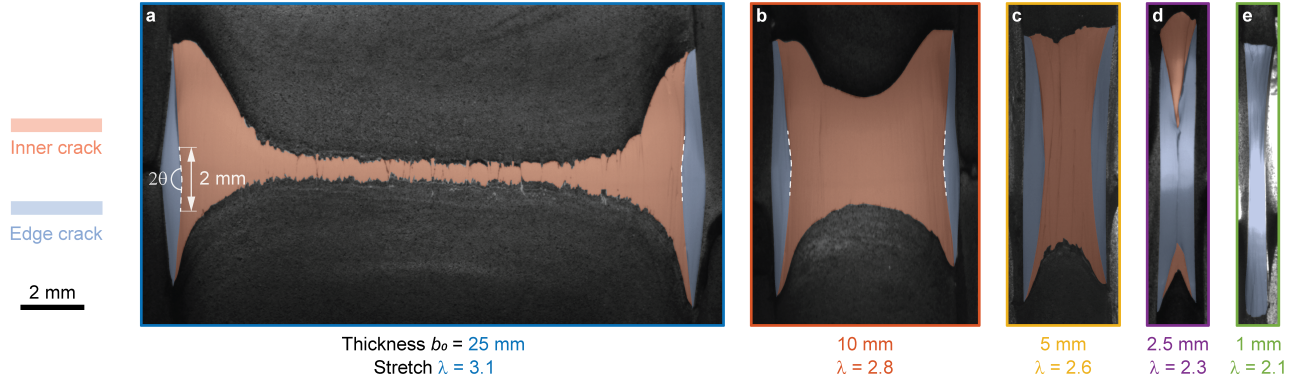


Supplemental Material Fig. 4. Diamond structures in T-peel tests on Ecoflex 00-30 samples. The images show the same images given in Fig. 3 in the article, but tinted blue and red to highlight areas produced by edge cracks and inner cracks, respectively. The dashed lines denote the tips of the diamond shapes, which we characterize to measure $\theta$.
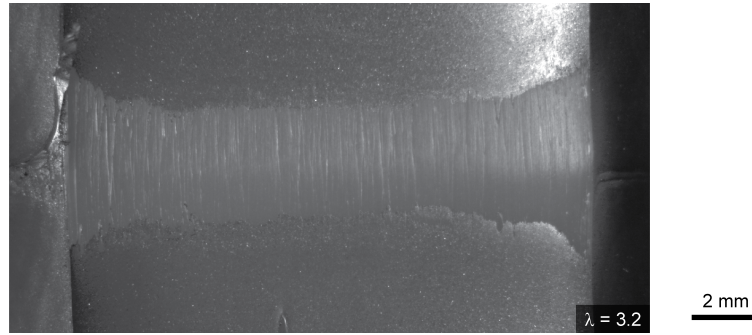


Supplemental Material Fig. 5. A snapshot of the T-peel test for Vytaflex 40, showing newly opened fracture surface, when the stretch $\lambda = 3.2$. The sample thickness $b_0 = 25$ mm. We do not see a recognizable diamond structure.